A geometric approach to modeling microstructurally small fatigue crack formation: III.

Development of a semi-empirical model for nucleation

A geometric approach to modeling microstructurally small fatigue crack formation: III. Development of a semi-empirical model for nucleation

J D Hochhalter[1,6]**, D J Littlewood**[2]**, M G Veilleux**[3]**, J E Bozek**[3]**,
A M Maniatty**[4]**, A D Rollett**[5] **and A R Ingraffea**[3]

[1] NASA Langley Research Center, Hampton, VA 23681-2199, USA
[2] Sandia National Labs, Albuquerque, NM 87185
[3] Cornell Fracture Group, Cornell University, Ithaca, NY 14853, USA
[4] Rensselaer Polytechnic Institute, Troy, NY 12180, USA
[5] Department of Materials Science and Engineering, Carnegie Mellon University,
Pittsburgh, PA 15213, USA

E-mail: Jacob.D.Hochhalter@nasa.gov

Abstract

It has been observed during fatigue cracking of AA 7075-T651 that a small
percentage of Al_7Cu_2Fe particles crack during manufacturing or very early in
their life. Some of the cracked particles eventually nucleate cracks into the
surrounding microstructure, and among these the number of cycles required
for nucleation varies widely. It is important to comprehend the mechanics
underpinning the observed variation so that the subsequent propagation stage
can be accurately modeled. To this end, finite element models of replicated
grain and particle geometry are used to compute mechanical fields near
monitored cracked particles using an elastic–viscoplastic crystal plasticity
model that captures the effect of the orientation of the grains near each
monitored particle. Nonlocal, slip-based metrics are used to study the
localization and cyclic accumulation of slip near the cracked particles providing
mechanics-based insight into the actuation of the nucleation event. A high
slip localization and cyclic accumulation rate are found to be a necessary, but
not sufficient, condition for nucleation from cracked particles. A sufficient
local driving stress must also be present, which is strongly dependent on the
local microstructure and accumulated slip. Furthermore, the simulation results
elucidate a quantitative relationship between the slip accumulated during fatigue
loading and a consequential reduction of the critical local driving stress for
nucleation, providing a physical basis for the fatigue damage concept. The

[6] Author to whom any correspondence should be addressed. Durability and Damage Tolerance Branch, NASA Langley
Research Center, MS 188E, Hampton, VA 23681-2199, USA.

observed nucleation direction is orthogonal to the computed local maximum tangential stress direction, as expected for this alloy. The main result is a semi-empirical model for the number of cycles required for nucleation, which is dependent on the maximum tangential stress and cyclic slip-accumulation rate near a cracked particle.

(Some figures in this article are in colour only in the electronic version)

1. Introduction

Fatigue life prognosis is currently limited in its ability to incorporate microstructurally small fatigue crack (MSFC) growth. However, in high-cycle fatigue, this regime accounts for a majority of the fatigue life for structural components (Brockenbrough *et al* 1994, Suresh 1998, Fan *et al* 2001). Improved insight regarding the behavior of metals under fatigue loading reduces uncertainty in growth models and, consequently, reduces cost through longer inspection intervals, improved design, and delay or elimination of component retirement. Furthermore, improvements in modeling plasticity and fracture within a microstructure provide a means to test virtual microstructures to determine the characteristics that promote fatigue resistance, which can streamline design of improved, fatigue resistant, materials. These improvements in fatigue modeling and simulation rely on the continual refinement in understanding of the mechanisms that drive fatigue cracking and the inherent material mechanisms that resist it. The reader is directed to McDowell (2007), McDowell and Dunne (2010) and Chan (2010) for recent encompassing reviews of microstructure-sensitive fatigue crack formation and modeling.

The MSFC phase is strongly dependent on microstructural heterogeneities and, as such, is governed by mechanisms that differ from those in long cracks, e.g. similitude does not apply. Consequently, several studies have incorporated a multistage decomposition of fatigue life into a superposition of models for incubation, microstructurally small crack growth and long crack growth (McDowell *et al* 2003, McDowell 2007, McDowell and Dunne 2010). Therein, 'incubation' is the aggregation of the appearance of a fatigue crack plus the crack growth required to extend beyond the crack-initiating feature. Advances in high-resolution characterization and computational capability have provided the means to decompose further the stages of MSFC, which necessitates slightly modified terminology. Herein, as in the previous papers in this series, 'incubation' is decomposed into three stages which can be distinguished during physical experiment: incubation, nucleation, and early microstructurally small crack propagation, as defined in figure 1.

The MSFC phase decomposition considered in this work is motivated by recent observations by Payne *et al* (2010). In the notch root of aluminum alloy (AA) 7075-T651 double-edge notched (DEN) specimens, Payne observed, as have many researchers, that cracking of Al_7Cu_2Fe particles was the first mechanism of consequence in the formation of MSFCs (Grosskreutz and Shaw 1969, Bowles and Schijve 1973, Kung and Fine 1979, Xue *et al* 2007b). This stage is termed incubation because of the relatively long cycle lag before the next stage, nucleation, is actuated. The nucleation event is defined by the extension of a crack, initially contained within a particle, into the surrounding alloy matrix. Microstructurally small propagation is defined as the early stage of fatigue crack growth in which microstructural features still play a dominant role in controlling crack shape and rate of growth. The experimentally observed cycle lags among the three stages are illustrated in
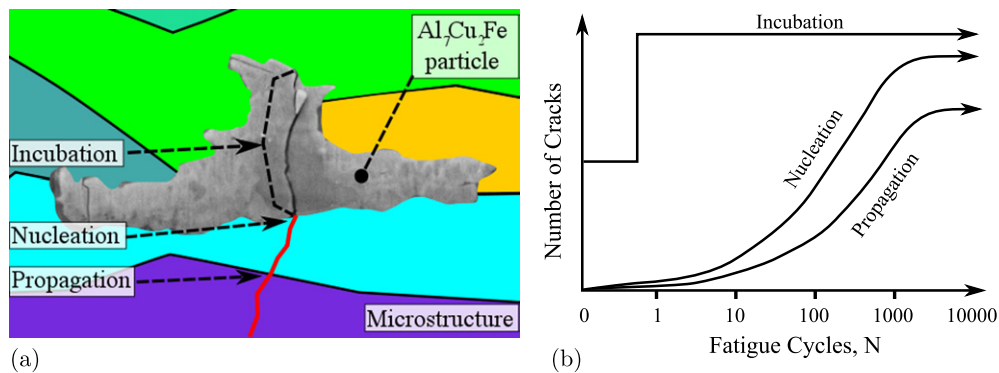
Figure 1. Illustration of and physical reasoning for the decomposition of the MSFC phase into three stages: incubation; nucleation and propagation. (*a*) Incubation is defined as the cracking of an Al_7Cu_2Fe particle, nucleation occurs when the incubated crack crosses the particle/grain interface, and propagation is the navigation of the crack through the microstructure. (*b*) Incubation occurred either before loading or upon the first load cycle; a significant time lag occurred before incubated cracks nucleated; and propagation occurred shortly after nucleation (Payne *et al* 2010).

figure 1(*b*). Each of these stages is governed by distinct mechanisms and is strongly dependent on the local microstructure.

The development of a mechanistic and probabilistic MSFC simulation methodology is presented throughout this series of papers. In the first paper of the series, Bozek *et al* (2008) developed a methodology to provide a statistical distribution of Al_7Cu_2Fe particles that are likely to incubate a crack, given distributions of particle shape, particle size and surrounding grain orientation. In that first paper, an elastic–viscoplastic crystal plasticity model for AA 7075-T651, which accounts for Orowan's mechanism for dispersion hardening that occurs in this peak-aged alloy, is used to capture the effect of grain orientation. That crystal plasticity model is used throughout the present series. In the second paper of this series, five nonlocal slip-based metrics were defined to study nucleation, and numerical issues and physical validity were investigated (Hochhalter *et al* 2010). It was found that a mesh-insensitive solution could be attained with refinement and a nonlocal query (1 μm from a crack front) of the slip fields. However, no conclusion could be made as to the physical validity of using accumulated slip alone to model the number of cycles required to nucleate an incubated crack.

This paper, the third in the series, describes the development of a semi-empirical nucleation stage model. To this end, finite element models were generated by replicating the observed microstructure surrounding cracked Al_7Cu_2Fe particles. The evolution of these incubated cracks was closely monitored during fatigue loading, providing observational data on the number of cycles required to nucleate the incubated cracks, and their initial propagation direction. Simulations of cyclic loading (with applied strains equivalent to those in the DEN notch root) of the replicated-microstructure models were used to compute stress concentration and slip localization and accumulation near the incubated cracks. A description of the process by which the replicated finite element models were generated is given in section 2.

It is shown in section 3 that accumulated slip is a necessary, but not sufficient, condition for nucleation. Furthermore, simulation results of the replicated-microstructure models elucidate that the critical local stress required to drive nucleation reduces as slip is accumulated, providing a physical basis for the concept of fatigue damage. Based on these results, a semi-empirical model for the required number of cycles for nucleation (given that the necessary condition for nucleation is met) of an incubated crack, and its direction, is developed in section 4. To

employ the model, finite element analysis is required to compute stress concentration, slip localization and slip-accumulation rate. Lastly, some of the limitations of, and alternative methods for, simulating the stages of MSFC using elastic–viscoplastic crystal plasticity within the finite element framework are given in section 5. The objective of developing fatigue models that explicitly incorporate the intrinsic and extrinsic effects on MSFC behavior is that more generally applicable, load and geometry independent models can be used. This detailed treatment of the mechanics underpinning the MSFC phase is made possible by improvements in materials characterization, physics-based constitutive models, and parallel-computation. An immediately useful outcome is the possibility to assess observed variability that arises from microstructural variability. Before describing this work, a brief review of relevant experimental observations and simulation studies of microstructure effects on MSFCs is given.

1.1. Prior experimental observations

Many researchers have summarized observations of MSFC behavior in many metallic materials in the literature. Among all of the studies, two fundamental questions recur: when does plastic deformation occur and when does cracking occur? From the wealth of empirical data gained from decades of experimentation, the fatigue community has been gaining insight into particular instances of this question, but a fundamental comprehension of the mechanics is often lacking. The main threads in the empirical knowledge base are drawn into two topics for preliminary discussion here: the formation of microcracks at microstructural features, and the localization and accumulation of plastic deformation near microcracks.

It is commonly observed that microstructural heterogeneities, such as second-phase particles or grain boundaries, are microcrack-forming features. Microstructural heterogeneities are likely crack formation sites partially because of the localization and accumulation of plastic deformation that they induce (McClintock 1968). Among the many observations of MSFC, it is commonly noted that when second-phase particles are associated with incubation sites, relatively large particles are more likely to incubate a crack. Laz and Hillberry (1998) studied the MSFC phase in AA 2024-T3 and found that relatively large, $\geqslant 58 \, \mu m^2$, Al_7Cu_2Fe particles were crack incubation sites. Bowles and Schijve (1973) provided experimental observations of the effect of constituent particles in AA 2024-T3. They concluded that large plastic strains led to particle–matrix debonding or cleavage of particles, the preference of which is apparently determined by particle geometry, spacing, composition and the alloy processing method. They also observed that the early propagation direction of microstructurally small cracks is markedly affected by the geometry of constituent particles. Kung and Fine (1979) observed that fatigue cracks initiated on coarse slip lines at relatively high applied cyclic stress in AA 2024-T3 and at lower applied cyclic stress the incubation was associated with consitituent particles. Grosskreutz and Shaw (1969) observed that constituent particles were exclusively associated with fatigue crack incubation in AA 2024-T4, even in the presence of concentrated slip bands. Patton *et al* (1998) studied the critical microstructural mechanisms governing the MSFC phase in AA 7010. They observed that fatigue crack incubation sites were either Al_7Cu_2Fe or Mg_2Si particles and, furthermore, that crack incubation and nucleation were influenced by the local crystallographic texture.

Slip behavior is also commonly noted to be a dominant mechanism in MSFC formation. Horton and Ohr (1982) monitored dislocation emission in single-crystal Al using transmission electron microscopy (TEM) and noted that dislocations accumulate near the crack upon loading, but that crack propagation was abrupt, during which the crack was sharp and dislocations were not emitted. McEvily Jr and Johnston (1967) recorded observations of the interplay between slip behavior and fatigue in an Fe–Si alloy, and compared and contrasted with observations

made during fatigue of a variety of basic alloys. In particular, they made observations of stage-I fatigue cracking, when cracks form and grow along the crystallographic planes with the highest shear stress, versus stage-II cracking, when the cracks form and propagate along the direction normal to the maximum tensile stress. It was observed that difficulty in cross-slip led to an increased crack formation frequency for stage-I cracks, apparently due to slip localization on a particular system. Conversely, ease of cross-slip enabled diffusion of slip localization on individual slip systems and stage-I crack formation frequency decreased. They concluded that diffuse slip physically restricted tensile stress concentrations, which, in turn, reduced the likelihood of stage-I cracking.

The aging process of metallic alloys affects the size and strength of the hardening precipitates, which, in turn, affects slip localization and cyclic accumulation, and MSFC behavior. Templin (1954) observed that 'weakening' of AA 2024-T3 (under-aged) and AA 7075-T6 (peak-aged) under low-cycle fatigue occurred due to dislocation accumulation on slip planes and subgrain structure formation. Garrett and Knott (1975) studied fatigue cracking in pure Al–Cu alloys. They observed that, in the under-aged condition, crack growth navigated low-index crystallographic planes (stage-I behavior), but only at the specimen surface where plastic restraint was low. In the peak and over-aged conditions, they found that growth did not correspond to low-index crystallographic planes, even at the specimen surface. Laz and Hillberry (1998) studied the MSFC phase in AA 2024-T3 (under-aged) and observed that crack nucleation from second-phase particles was stage-I. Santner and Eylon (1979) studied MSFC in AA 7075-T651, the same peak-aged alloy investigated here, but in an inert environment, and observed that fracture initiated on {1 1 1} slip planes (stage-I cracking). However, other researchers have observed that the environment has a strong affect on whether stage-I or stage-II cracking occurs: a normal air environment promotes stage-II fatigue cracking, while an inert environment promotes stage-I fatigue cracking (Pelloux 1969).

1.2. Prior modeling work

Idealized, analytical models of dislocation pile-ups at intermetallic particles were developed and used in early investigations attempting to better understand the effect of microstructure on incubation and nucleation. Chang *et al* (1979) and Morris and James (1980) incorporated effective shear stress—assumed to be constant within each grain—into Monte Carlo simulations, and they predicted that nucleation would occur at progressively smaller particles throughout fatigue life. Also, it was found that crystallographic orientation was a major factor in the probability of nucleation of an incubated crack, and that the number of cycles required to nucleate a crack was much higher than that of incubation, which is consistent with the observations illustrated in figure 1(*a*). Tanaka and Mura also developed a dislocation pile-up model assuming that nucleation occurs when a critical strain density is attained. They have shown that this model yields the Coffin–Manson relationship for fatigue crack nucleation and a Petch-like relationship of grain size and fatigue strength (Tanaka and Mura 1981, 1982a,b, 1984). The Tanaka–Mura model agrees with that of Morris and James in that it is predicted that relatively large particles will nucleate cracks earlier than smaller particles (Tanaka and Mura 1982b). Chan (2003) modified the Tanaka–Mura model for crack nucleation based on dislocation pile-up for stage-I growth by incorporating crack size and microscale-dependent parameters. The crack length at nucleation is modeled as the alignment of dislocations along a slip system, each contributing a Burgers vector magnitude to the crack length. For crack nucleation in a grain, the Taylor factor, grain diameter, slip-band width, and surface energy were incorporated; however, the Taylor factor was fixed at 2, and the slip-band width and surface energy were constant parameters calibrated to experimental

data. They found that the predicted crack initiation sizes were several orders of magnitude lower than those observed experimentally.

Application of computational mechanics, especially prevalent over the last decade, has enabled refinements in modeling the effects of grain orientation, grain boundary misorientation, constituent particles, etc, on MSFC behavior. Even so, a fundamental mechanics basis describing the sequence of plastic deformation and crack growth is still lacking. Recent literature is illustrative of the focus that is being placed on such a mechanics-based understanding by the fatigue research community. A brief highlight of some microstructure-dependent modeling and simulation studies is given here. The reader is directed to McDowell and Dunne (2010) for an encompassing review of recent computational modeling of MSFC in aluminum and nickel-based alloys.

Localized deformation in the neighborhood of second-phase particles was modeled by Gall *et al* (2001), Xue *et al* (2007a) and Zhang *et al* (2009). Gall *et al* (2001) studied the relative effect of cracked and debonded particles on MSFC in cast alloy A356. Cracked and debonded particles were modeled in a 2D isotropic elastic–plastic model and it was found that strain localization was intensified near the debonded particles, which supports observations of MSFC in cast alloy A356. Xue *et al* (2007a) used an internal state variable, isotropic, elastic–plastic constitutive model for nonlocal calculation of the maximum plastic shear strain amplitude, which was used to inform a modified Coffin–Manson model for the number of cycles required for incubation, nucleation, and early propagation. In that work, parameters for considering grain orientation and size effects were included, but ultimately not used because of lack of information on the complex effects that these factors might have. Zhang *et al* (2009) studied fatigue crack nucleation from inclusions within an isotropic, elastic–plastic, rate-independent material using 3D finite element modeling. These, along with several other informative studies (McDowell *et al* 2003, Shenoy *et al* 2005, Przybyla *et al* 2010), have developed 'fatigue indicator parameters,' e.g. cyclic plastic shear strain accumulation or the Fatemi–Socie metric (Fatemi and Socie 1988, Fatemi and Yang 1998), to model MSFC driving forces.

Several researchers have considered the effect of grain orientation and geometry on localized, heterogeneous deformation and related that to MSFC behavior. Most previous studies in the literature have considered the local orientation, but not interactions with the surrounding microstructure, i.e. single-crystal simulations. Bennett and McDowell (2003) considered the effect of crystallographic orientation on three proposed fatigue crack indicator parameters. They modeled an idealized, planar polycrystal, without inclusions, subjected to several different cyclic loading histories, considering a combination of plane strain tension/compression and shear. Johnston *et al* (2006) added to these studies by simulating intragranular crack growth in AA 7075-T651 using 3D finite element modeling. Similarly, Potirniche and Daniewicz (2003) found that plastic zone shape and size, as well as crack-tip opening, were strongly influenced by grain orientation. Wang *et al* (2009) published results of simulations of a MSFCs near the grain boundary in a bicrystal, where several model parameters were considered in a design of experiments study.

Observations of MSFCs during experiment have been closely tied with corresponding finite element simulations in studies of both single and polycrystal nickel-based alloys. Flouriot *et al* (2003) generated 3D, single-crystal finite element models of a nickel-based superalloy and validated simulated fields with experimentally observed deformation modes. They concluded that the computed deformation compared well with the experiment, outside of a core region directly surrounding the crack front where intense discrete slip lines were not captured in the finite element modeling. Manonukul and Dunne (2004) generated a 2D finite element model of a nickel-based polycrystalline alloy and computed slip accumulation throughout. A critical accumulated slip rule was found to correspond with the Coffin–Manson

relationship in low-cycle fatigue. Dunne *et al* (2007) replicated, as a finite element model, the grain geometry and orientation using electron back-scatter diffraction (EBSD) of a nickel-based alloy with prismatic grains. It was found that the crack formation corresponds to locations of highly localized slip, as predicted from the finite element model. Arakere *et al* (2009) generated 3D models of a single-crystal nickel-based alloy modeled as an elastic anisotropic material and showed that, even with a simplified model for crystal response, the slip-localization directions could be predicted near a crack front.

Historically, the capability to make detailed observations of fatigue behavior at the microscale has surpassed the capability to model the sequence of mechanisms underpinning this behavior, which has made physical inference of the observations difficult. The detailed simulation of MSFC, characteristic of the last decade, has incorporated the mechanics of various heterogeneities and slip behavior to aid the formulation of more accurate, fundamental MSFC models. Improvements in the accuracy of deformation models near a microstructurally small crack continue to improve the ability to interpret observations and reduce uncertainty in fatigue life modeling approaches.

2. Experiment and replicated-microstructure modeling

For this study, two fatigue experiments on AA 7075-T651 DEN specimens were performed to provide observations of the MSFC phase. AA 7075-T651 is a precipitation hardened alloy, and the specimens investigated in this study were found to have the following chemical composition (by weight): Zn 5.7%, Mg 2.5%, Cu 1.7%, Cr 0.19%, Fe 0.26%, Si 0.06%, Mn 0.03%, Ti 0.02%, Ni 0.003% and V 0.006% (Payne *et al* 2010). The T651 designation indicates that the alloy was solution heat treated, stress-relieved by stretching and artificially aged. Within the notch root of one DEN specimen, 1423 Al_7Cu_2Fe particles were monitored throughout 3000 cycles of $R = 0.1$, constant amplitude loading applied at 1 Hz in the rolling direction (RD). The observation window at the monitored notch root was 1.50 mm × 0.50 mm in the normal direction (ND) and RD, respectively, figure 2. The loading and environmental conditions applied during the experiment emulated overload cycles near an aircraft wing-panel bolt-hole. A detailed description of these experiments is given by Payne *et al* (2010).

The experiment illustrated that the incubation stage in AA 7075-T651 occurs, almost exclusively, during manufacturing or the first half cycle of loading, but only in a small percentage of particles in a highly stressed region (Payne *et al* 2010). These observations are consistent with that of many others (Bowles and Schijve 1973, Murakami and Endo 1994, Laz and Hillberry 1998, Patton *et al* 1998, Xue *et al* 2007b, Weiland *et al* 2009). As stated above, the alloy was stress-relieved by stretching, which minimized residual stresses induced by heat treatment and rolling, but contributed to particle cracking. Crack nucleation occurred exclusively from incubated cracks and did so at a widely varying number of cycles. Cracks were observed to nucleate from approximately 73% of the monitored cracked particles, figure 3. This observation was also made by Weiland *et al* (2009) in a separate study.

From the 1423 particles monitored by Payne *et al* (2010), a subset of 11 particles of interest was selected for replication analysis. Figure 2 illustrates the observation window within which these 11 particles of interest were monitored, along with the relative locations of the particles. These particles were chosen because they collectively represent a cross section of five observed variables: size, aspect ratio, incubation during manufacturing or loading, the occurrence of nucleation and the number of cycles to nucleation, if it occurred, see table 1. Of the 11 particles, seven incubated a crack during the first load cycle, and four during manufacturing. Seven incubated cracks subsequently nucleated at a wide range of cycles, see table 1. Comparing and contrasting the data presented in table 1 illustrates that the particle
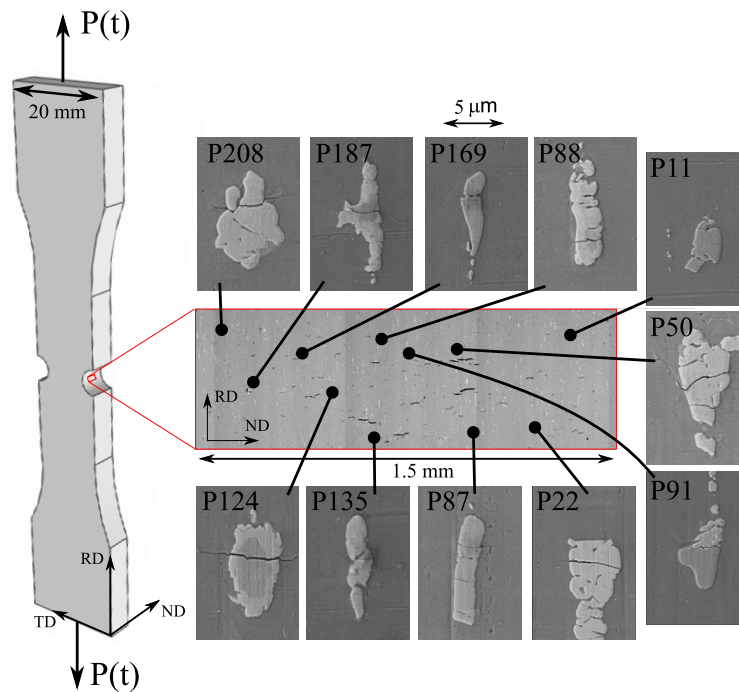
Figure 2. Observation window at the DEN specimen notch root where particles were monitored during cyclic loading. The 11 monitored particles that were chosen for replication simulations are illustrated, along with their location within the observation window.
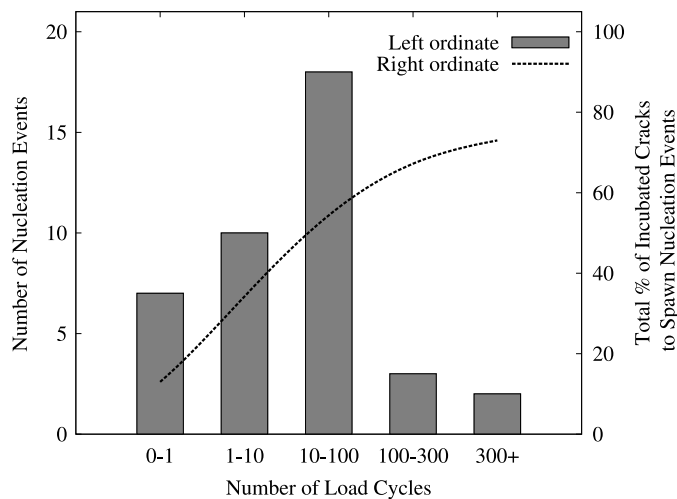
Figure 3. A histogram of the cycles at which nucleation events occurred for the AA 7075-T651 DEN specimen. Approximately 73% of the observed incubated cracks led to crack nucleation into a surrounding grain.

size and the number of cycles to nucleation are not directly correlated. Thus, particle size alone is not a sufficient metric for modeling crack nucleation and growth. This conclusion holds for the statistical analyses of the 1423 particle data set made by Payne *et al* (2010) and Harlow *et al* (2010).

Table 1. Summary of observations and measurements of the 11 particles of interest chosen for replication simulations. Incubation during cycle number '0' implies that it occurred prior to cyclic loading application.

Particle Id	ND × RD size (μm^2)	Incubation (cycle number)	Nucleation (cycle range)
P11	4 × 6	1	N/A
P135	1 × 6	1	N/A
P169	2 × 8	1	N/A
P88	3 × 9	0	N/A
P187	3.3 × 10	1	10–30
P91	5 × 8	1	10–30
P50	4 × 8	0	30–100
P124	6 × 6	0	100–300
P87	2 × 9	1	100–300
P208	5 × 8	0	300–1000
P22	2 × 10	1	300–1000

Finite element models were generated that replicate the measured grain, particle and crack geometry, and grain orientations based on orientation imaging microscopy (OIM) and scanning electron microscopy (SEM) images of subregions containing the 11 particles of interest. Grain boundaries were defined by misorientations $\geqslant 6°$. Figure 4 illustrates the processing of OIM data to generate replicated 3D finite element models. With the DEN specimen on a tilt stage in a SEM, EBSD was used to determine grain structure and orientation at the notch root, specifically in regions encompassing several particles of interest. The resulting images were 'wrapped,' figure 4(*a*), because of the stage tilt and curvature of the notch.

The Rhino3D® software was used to 'unwrap' these images, figure 4(*b*). After the OIM images were correctly aligned with the specimen RD, ND and transverse direction (TD) axes, a rectangular bounding box was superimposed and grains extending beyond the boundary were trimmed for boundary condition application, figure 4(*b*). In general, the bounding region was chosen to be approximately $100\,\mu$m $\times\ 50\,\mu$m (RD × ND), 10–20 times the typical dimensions of the particle of interest, which was centered in the bounding box. The grain boundaries around the constituent particles were often shadowed in the OIM data sets, which reduced accuracy when tracing the grain boundaries very near the particle. This occurs because second-phase particles are much harder than the neighboring alloy matrix, and as a result the particles protrude from the surface slightly after polishing. Another cause of the shadowing effect was due to the 70° tilt of the specimen with respect to the EBSD camera.

After the 2D microstructural geometry was unwrapped and clipped, geometrical checks were done for coherence along all interfaces and enclosure of each particle and grain region. Each enclosed region was associated with the measured average lattice orientation, unless the region was a particle, in which case the region was defined as isotropic. Since no microstructural geometry data could be acquired in the TD, the grain boundaries traced in the RD–ND plane were extruded $74\,\mu$m in the TD to be consistent with the 50th percentile of experimentally observed grain aspect ratios, figure 4(*c*). Similarly, each particle was extruded $3\,\mu$m in the TD in accordance with the 50th percentile of experimentally observed particle size in the TD. Extruding the geometry into the TD, in this way, results in a void behind each particle, which was filled in by the grain that had the most contact with the particle. Because of the lack of TD morphology data in this study, the following discussion is limited to the results computed at the free surface, where the morphology is known to be accurate. More accurate methods for determining 3D microstructure morphology, such as 3D x-ray tomography and
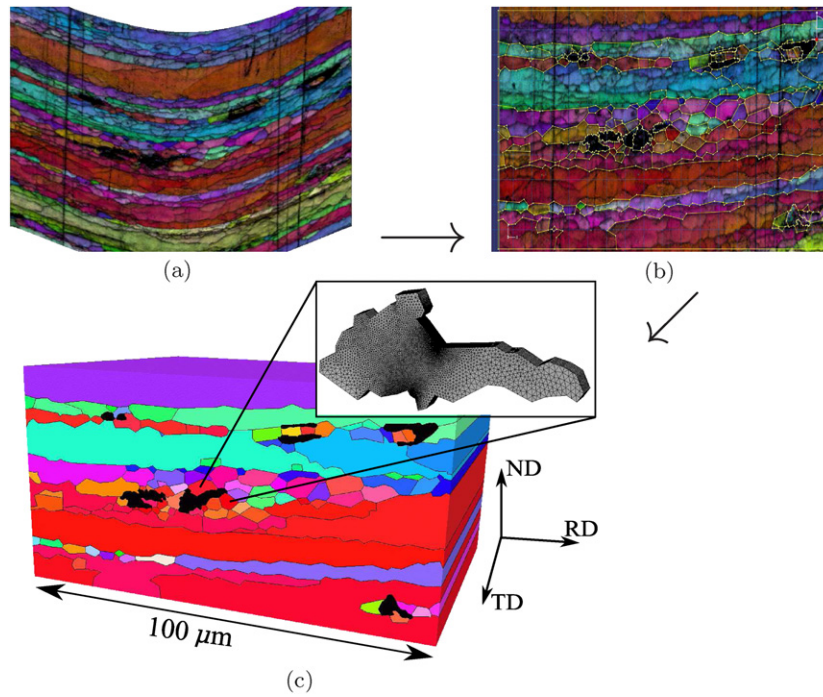
Figure 4. Process of creating the replicated-microstructure finite element models required 3 main steps: (*a*) obtaining the EBSD orientation map, (*b*) unwrapping, clipping, and outlining the grain boundaries and (*c*) extruding and meshing. This process is illustrated for a particle of interest, P22.

serial sectioning, are currently being developed and will be useful in more accurately replicating microstructural geometry, cf (Maire *et al* 2001, Brahme *et al* 2006, Hefferan *et al* 2009).

Cracks in the particles were geometrically represented and the geometry was meshed for finite element analysis. From the results of the previous nonlocal mesh convergence study by Hochhalter *et al* (2010), element edge lengths near the crack front were limited to ≤1% of the observable crack size. The meshed models range in size from 5–15 million degrees of freedom (about 1–4 million quadratic tetrahedra).

An elastic–viscoplastic crystal model implemented into a mixed finite element formulation with continuous quadratic displacement and discontinuous linear pressure interpolations on tetrahedral elements was used in the simulations here (Matouš and Maniatty 2004). The elastic–viscoplastic crystal model incorporates the twelve primary $\{1\,1\,1\}\langle 1\,1\,0\rangle$ slip systems for FCC crystals to accommodate plastic deformation. The plastic velocity gradient, $\hat{L}^{\mathrm{p}}$, is related to the rate of slip on the slip systems as

$$\hat{L}^{\mathrm{p}} = \sum_{\alpha=1}^{N_{\mathrm{s}}} \dot{\gamma}^{\alpha} P^{\alpha}, \tag{1}$$

where α denotes a specific slip system, N_{s} the total number of slip systems, $\dot{\gamma}^{\alpha}$ the slip rate on slip system α and P^{α} the Schmid tensor for slip system α. A power law relates $\dot{\gamma}^{\alpha}$ to the resolved shear stress on each slip system. The hardening behavior in the elastic–viscoplastic crystal model was derived based on the Orowan looping mechanism for precipitation strengthened alloys, which favors multi-slip. Detailed discussions of the elastic–viscoplastic crystal model are provided by Matouš and Maniatty (2004) and Bozek *et al* (2008). The elastic–viscoplastic crystal model used here does not employ a separate kinematic hardening term

to model the Bauschinger effect because the model was found to capture the Bauschinger effect observed in the data for AA 7075-T651 without any additional terms. It has also been shown by Tóth *et al* (2000) that the Bauschinger effect is predicted from polycrystal models without additional terms. The Al_7Cu_2Fe particles were modeled as linear elastic to failure because of observed brittle behavior and the nanoindentation measurements provided by LeDonne *et al* (2011).

A component-scale, elastic–plastic finite element analysis of the DEN specimen was completed and local strain fields were extracted to obtain an accurate description of the strain field local to each notch; a local peak strain of 1% and local minimum strain of 0.05% in the RD was computed (Fridline 2007). Any gradients in the displacement field used for boundary conditions were neglected. This entire microstructure replication process was automated via the ABAQUS® Python scripting interface, where construction of the 3D polycrystal, meshing, and application of material parameters and boundary conditions were completed. Each of the microstructural models were then subjected to 2.5 constant amplitude loading cycles, which was previously found to provide a first-order estimate of the rate of slip accumulation near the crack per cycle (Hochhalter *et al* 2010). The simulations were then performed using an in-house parallel finite element solver, which typically utilized 1000–4000 processor cores for 12–48 wall-clock hours per load cycle.

The objective of this detailed analysis is to develop a model to predict (1) which particles nucleate a crack into the surrounding matrix, (2) the load cycle at which nucleation events occur, and (3) the direction of nucleation. The simulations of replicated microstructures under cyclic loading enable physical inference of the observed variability in these three important elements of fatigue cracking. Comparison of the computed stress and slip fields near the incubated cracks that nucleated with those that did not nucleate provides insight into why nucleation occurs. Comparison of the computed stress and slip fields near those that nucleated relatively early with those that nucleated relatively late illustrates how local microstructure affects variability in number of cycles to nucleation.

3. Nucleation stage replicated-microstructure simulations

A basis for this study is provided by Hochhalter *et al* (2010), in which the numerical issues and physical validity of using cyclic accumulated slip alone to model the number of cycles required to nucleate an incubated crack were determined. It was made apparent in that initial investigation that slip-based metrics that characterize localization[7] and cyclic accumulation could be used to better understand nucleation. The orientation of grains surrounding a cracked particle was shown to affect whether a single or multiple slip-localization direction(s) were governing plastic deformation near the cracked particles. However, neither a model for the number of cycles required to nucleate an incubated crack nor a nucleation direction criterion could be determined by Hochhalter *et al* (2010) because of a lack of simulation data. In the following discussion, results of the various fatigue-loaded replication models, presented in section 2, provide the physical basis needed to develop a model for the number of cycles required to nucleate an incubated crack, and its direction.

3.1. Analysis of stress and slip-based metrics results

To study localization and cyclic accumulation of slip within the grains surrounding a cracked particle, five slip-based metrics (termed D_{1-5}) were defined by Hochhalter *et al* (2010). The

---

[7] *Localization* in this paper refers to localization of slip due to the presence of the crack. It does not refer to localization of slip on a particular system, nor does it refer to the formation of persistent slip bands.

metrics are motivated by observations regarding the effect of aging on slip system activity and the potential relationship to crack nucleation. These slip-based metrics extend the 'fatigue indicator parameters' concept, highlighted in section 1.1, in that they are used to indicate stages of MSFC, by explicitly incorporating slip localization and cyclic accumulation derived from crystal plasticity behavior. It was found in Hochhalter *et al* (2010) that for AA 7075-T651 (and the load level/ratio applied), D_{1-5} provided qualitatively similar results. Therefore, illustrations and discussion are limited to the D_1 and D_3 metrics since they provide the bounding concepts in such metrics.

Nucleation metrics D_1 and D_3 are functions of accumulated slip Γ^α, which is computed for slip system α as

$$\Gamma^\alpha = \int_0^t |\dot{\gamma}^\alpha| \, \mathrm{d}t, \tag{2}$$

where $\dot{\gamma}^\alpha$ is the slip rate on slip system α, which is integrated throughout the 2.5 loading cycles simulated here. Nucleation metric D_1 is then defined as the maximum value of Γ^α over all slip systems,

$$D_1 = \max_\alpha \Gamma^\alpha. \tag{3}$$

Nucleation metric D_3 is the total accumulated slip over all slip systems,

$$D_3 = \Gamma = \sum_{\alpha=0}^{N_s} \Gamma^\alpha. \tag{4}$$

In the replicated-microstructure models, the value of each slip-based metric was computed at each Gauss point in the model, resulting in a scalar field, see figure 5.

A nonlocal arc is then defined, along which the D_1 and D_3 metrics are queried from the underlying D_1 and D_3 scalar field, respectively, see figure 5. The nonlocal arc is simply a path that circumscribes a point on the crack front so that mesh insensitive, converged results can be obtained: divergence of fields at the crack front occurs with mesh refinement, as expected (Hochhalter *et al* 2010). Since slip does not occur in the Al_7Cu_2Fe particles, only the portion of the nonlocal arc that intersects a grain is considered.

The slip-based metrics obtained along the nonlocal arc were then regularized using either the maximum or average value to provide a practical means to compare and contrast among the localization and cyclic accumulation behavior of various sets of finite element results. The regularization of the nonlocal arc data to a single maximum or average value implies that the value represents the mechanics directly along the crack front. In other words, the nonlocal arc provides a means to compare converged values, while the regularization provides a single metric value characterizing a point on a microstructurally small crack front.

The nonlocal regularization techniques applied in this study are those presented in Hochhalter *et al* (2010), with modifications based on more recent observations. Hochhalter *et al* (2010) used 10–25% of the incubated crack size as the nonlocal arc radius. The lower bound was set as a result of divergence of fields very near the crack front. The upper bound was set to ensure that effects of the presence of the crack were considered. However, the use of continuum crystal plasticity, without consideration of gradient effects, is probably not reliable within $\approx 1\,\mu$m from the crack front. Therefore, a lower-bound, nonlocal arc radius of $1\,\mu$m is used in this study. Furthermore, numerical convergence is maintained with this lower bound since none of the incubated crack sizes are greater than $10\,\mu$m.

Instead of simply taking the maximum value along the nonlocal arc, the D_1 values at the location of maximum cyclic accumulation rate are considered. For D_3, the average value along the nonlocal arc is taken. The nonlocal maximum value of D_1 emphasizes
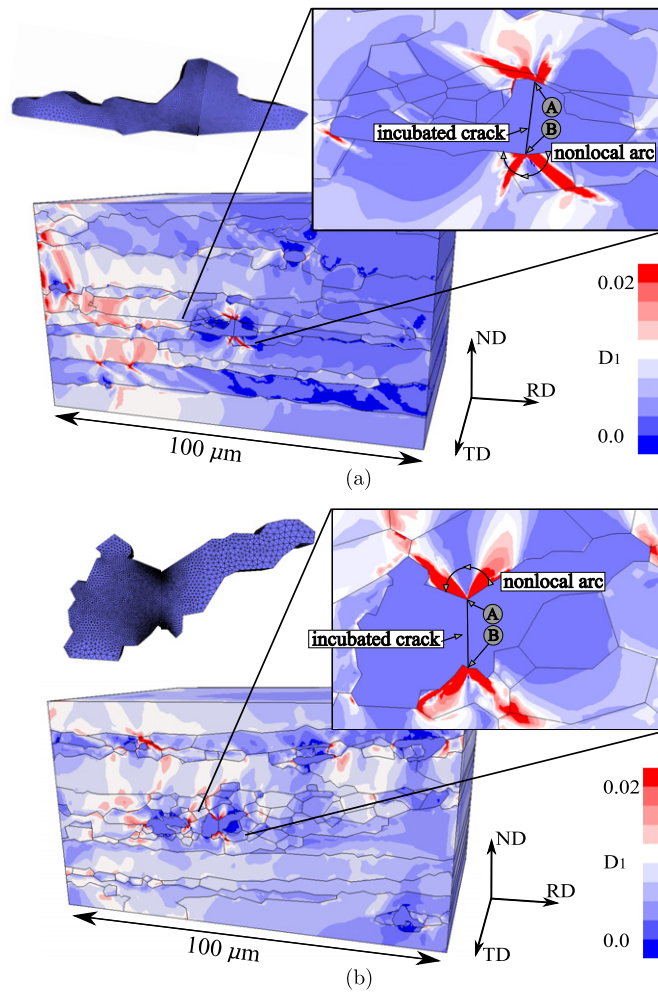
Figure 5. Computed D_1 contours at the peak of the 3rd load cycle with magnified view in the neighborhood of the cracked particles, (*a*) P187 and (*b*) P22. The meshed particles and nonlocal arc with radius 1μm, along which results fields were queried, are also illustrated.

the effect of localization of slip near the crack, while the nonlocal average value of D_3 emphasizes the effect of homogenization of slip near the crack. Analyzing these two metrics and regularization methods provides results at the bounds of the concept of these slip-based metrics and their nonlocal regularization. Briefly, nonlocal average of the Fatemi–Socie metric (Fatemi and Socie 1988) is also discussed because of its frequent usage throughout the literature.

A shorthand nomenclature is used while illustrating and discussing results from the replication simulations. First, to distinguish between a metric that is the result of one of the regularization techniques and the raw metric data along a nonlocal arc, a right superscript will be added to a field variable being regularized, e.g. $\sigma_{\theta\theta}^{\max}$ or D_3^{avg}. The right subscript on a field variable denotes the variable identifier and when a critical value of the field variable is referenced, a 'cr' is placed in the left superscript.

For brevity, some illustrations are limited to the results of the two monitored particles that bound the observed number of cycles to nucleation, P187 and P22, recall table 1. Figure 5

13
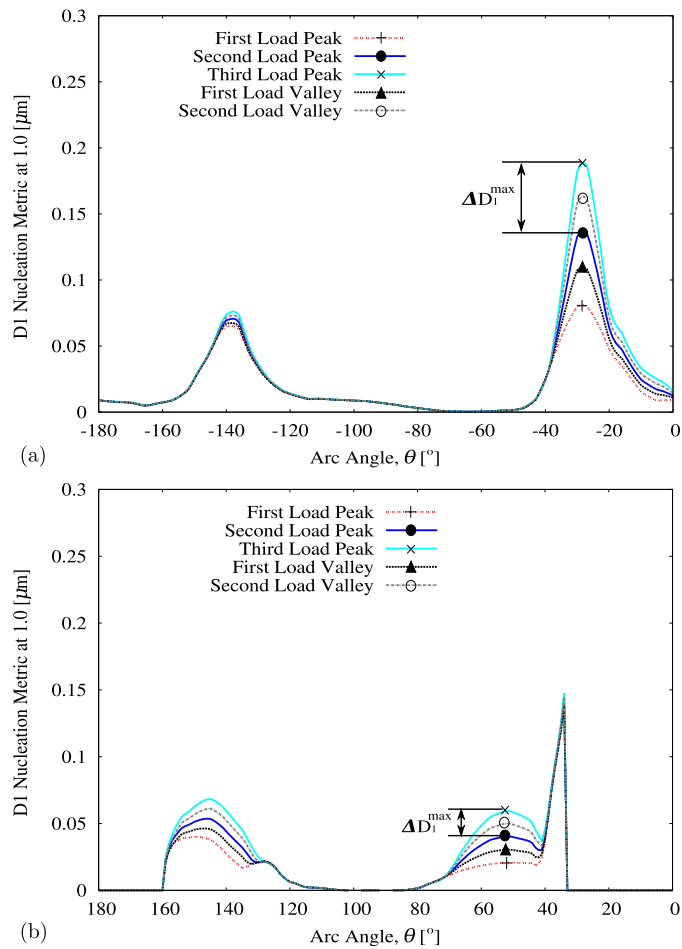
Figure 6. D_1 along the nonlocal arc—at 5 different times during the cyclic loading—about the point on the incubated crack front at which nucleation was first observed to occur from (*a*) P187 and (*b*) P22.

illustrates the D_1 scalar fields in the P187 and P22 replication models at the third simulated load peak (the end of the simulation). The heterogeneity in the slip field, especially the localization near the incubated crack, is immediately obvious in figures 5(*a*) and (*b*). D_1, D_3 and $\sigma_{\theta\theta}$ were queried along the nonlocal arc: $\sigma_{\theta\theta}$ is the component of stress tangential to the nonlocal arc at any point along it. Considering only the front RD–ND surface, there are 2 points where the incubated crack front intersects the free surface, illustrated by points A and B in figures 5(*a*) and (*b*). The nonlocal data presented here correspond to the point at which D_1 and D_3 accumulated at the highest rate.

Figures 6 and 7 provide the results of sampling the D_1 and D_3 fields along the nonlocal arc in P187 and P22 (at the point where nucleation first occurred), which are illustrated in figure 5. The nonlocal arcs are oriented such that $\theta = 0°$ is aligned with the RD and counter-clockwise movement along the arc is positive. These plots illustrate the locations of slip localization and cyclic accumulation that result from the cyclic loading and proximity to the incubated crack. It is evident that the D_1 and D_3 metrics provide qualitatively similar results; the computed global directions of slip localization and accumulation are equivalent. The D_3 metric values tend
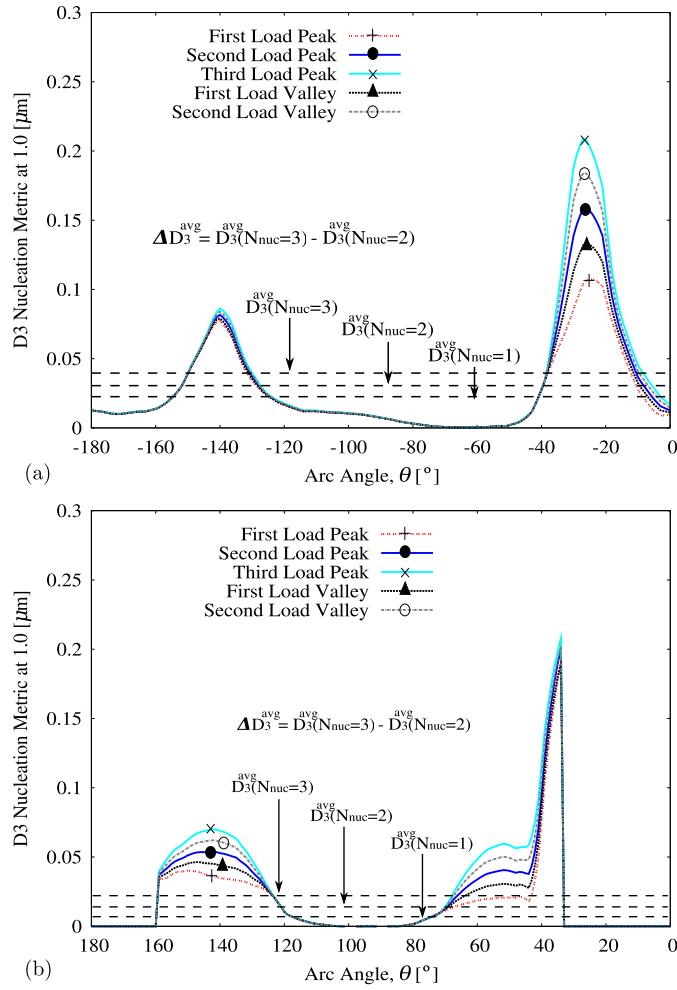
Figure 7. D_3 along nonlocal arc—at 5 different times during the cyclic loading—about the point at which nucleation was first observed to occur from (*a*) P187 and (*b*) P22. N_{nuc} is the number of cycles after incubation.

to be slightly higher than the D_1 metric values indicating some multiple-slip system activity, for the two models illustrated, as expected for this alloy. Also, the localization and cyclic accumulation are dependent on grain orientation and particle and grain geometry. For points along the nonlocal arc that lie in a particle region, the values of the slip-based metrics are set to zero, since the metrics are undefined within the isotropic elastic particles. The ΔD_1^{max} and ΔD_3^{avg} are the incremental increase of the regularized nonlocal metrics between the second and third load peaks and should not be confused with the increment between mininum load and peak load, see figures 6 and 7.

Comparing simulation results of those particles observed not to nucleate, table 2, with those observed to nucleate, table 3, illustrates that $\sigma_{\theta\theta}^{\text{max}}$ does not provide a valid criterion for which incubated cracks are likely to nucleate. However, it is also found by comparison of tables 2 and 3 that the values of ΔD_1^{max} near the incubated cracks that did not nucleate are significantly lower than those that did nucleate. This implies that the slip-based nucleation metrics provide a valid criterion for which incubated cracks are likely to nucleate: $\Delta D_1^{\text{max}} = 0.02$ was observed

Table 2. Summary of the replication simulation results for the four monitored particles that incubated a crack, but the incubated crack did not nucleate. The table contains $\Delta D_1^{\mathrm{max}}$ and $\sigma_{\theta\theta}^{\mathrm{max}}$ for each. Since nucleation was observed not to occur from these particles no linearly projected value of this metric can be provided. The values of $\sigma_{\theta\theta}^{\mathrm{max}}$ are presented for the first load peak.

| Particle Id	Accumulation rate $(\Delta D_1^{\mathrm{max}})$	$\sigma_{\theta\theta}^{\mathrm{max}}$ (MPa)
P135	1.6E−4	660
P169	3.5E−3	882
P11	2.0E−2	708
P88	0.0E+0	533

Table 3. Summary of the replication simulation results for the seven monitored particles that incubated a crack, and the incubated crack subsequently nucleated. The table contains $\Delta D_1^{\mathrm{max}}$, and its linearly projected value at the observed cycle range of nucleation, and $\sigma_{\theta\theta}^{\mathrm{max}}$ for each. The values of $\sigma_{\theta\theta}^{\mathrm{max}}$ are presented for the first load peak.

Particle Id	Cycle range of nucleation	Accumulation rate $(\Delta D_1^{\mathrm{max}})$	Linearly extrapolated (*lower*)	(*upper*)	$\sigma_{\theta\theta}^{\mathrm{max}}$ (MPa)
P187	10–30	4.2E−2	5.07E−1	1.4E+0	820
P91	10–30	5.3E−2	5.58E−1	1.62E+0	776
P50	30–100	2.9E−2	9.13E−1	2.93E+0	628
P124	100–300	2.0E−2	2.0E+0	5.9E+0	583
P208	300–1000	2.4E−2	7.3E+0	2.4E+1	535
P22	300–1000	7.0E−2	2.13E+1	7.03E+1	496
P87	300–1000	9.0E−7	2.6E−2	2.7E−2	606

to be the threshold value in this series of simulations. Note P87 is an 'outlier': according to results of slip-accumulation rate, P87 should not have nucleated. This discrepancy is attributed to a microvoid present at the point where the incubated crack in P87 met the grain boundary; this microvoid was not captured in the replicated model containing that particle. It is evident from table 3, however, that there is no direct correlation between $\Delta D_1^{\mathrm{max}}$ and the observed number of cycles to nucleation. In other words, the slip-based metrics provide a necessary, but not sufficient, condition for nucleation.

There is, however, a direct correlation between the magnitude of $\sigma_{\theta\theta}^{\mathrm{max}}$ near each particle and the observed number of cycles to nucleation for the particles with $\Delta D_1^{\mathrm{max}}$ above the threshold, table 3. The driving stress along the nonlocal arc, figure 8, varies among the replication simulations due to the microstructure surrounding each of the cracked particles, and those under relatively high stress nucleate earlier than those under a relatively low stress. This observation is analogous to the commonly observed macroscopic S-N fatigue behavior and this microstructural variability in driving force may lead to the variability commonly seen in macroscopic S-N behavior.

Hochhalter *et al* (2010) showed that the slip-based metrics could be linearly projected over a number of cycles as a first-order approximation, since a constant ΔD_{1-5} was found to occur after the first load cycle. To linearly extrapolate the slip-based metrics, a finite element simulation is needed to compute the value at the first peak and the subsequent constant accumulation rate. These values were calculated from the simulation results of the seven monitored particles that nucleated a crack; table 3 summarizes the linearly projected values to the observed cycle range of nucleation. Note that since observations of the microstructure were not made after every load cycle, only a range in which nucleation occurred is known, e.g. P187 had not nucleated a crack by 10 load cycles, but had by 30 load cycles.
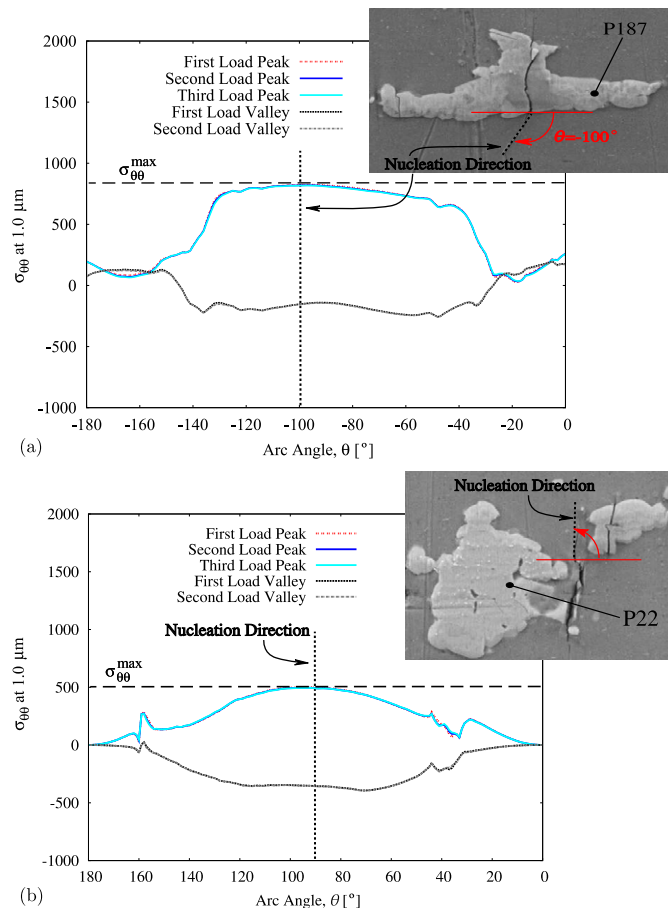
Figure 8. The computed tangential stress with respect to the nonlocal arc, $\sigma_{\theta\theta}$, about the point at which nucleation was first observed to occur from (*a*) P187 and (*b*) P22.

To this point, analysis of the computational results has led to two main conclusions: that the computed magnitude of slip localization and cyclic accumulation provides a valid metric for determining which incubated cracks will nucleate, and the computed tangential stress local to the incubated crack provides a valid metric for the number of cycles required to nucleate a crack. The aggregation of these two main points is illustrated in figures 9 (*a*) and (*b*). These figures illustrate that $^{\mathrm{cr}}\sigma_{\theta\theta}^{\max}$ decreases as the projected values of $D_1^{\max}$ and D_3^{avg} increase, and that the relation is power-ruled. The values of $\sigma_{\theta\theta}^{\max}$ and the projected $D_1^{\max}$ and D_3^{avg} values to the observed cycle of nucleation provide the critical relationship for nucleation, which is shown in figure 9. In addition, qualitatively similar results occur when the accumulated slip is modeled using $D_1^{\max}$ or D_3^{avg}. Quantitatively similar $D_1^{\max}$ and D_3^{avg} results are expected for nucleation in many under-aged alloys or an inert environment, where persistent slip-band cracking is more predominant.

For the alloy, environment, and loading being studied here, it is expected that the nucleation of the incubated crack into the surrounding grain will be a stage-II event. This is supported by a recent in-depth study of the correlation of crack propagation path and crystallographic systems for AA 7075-T651 by Gupta (2009), which indicates that there is no stage-I growth

17
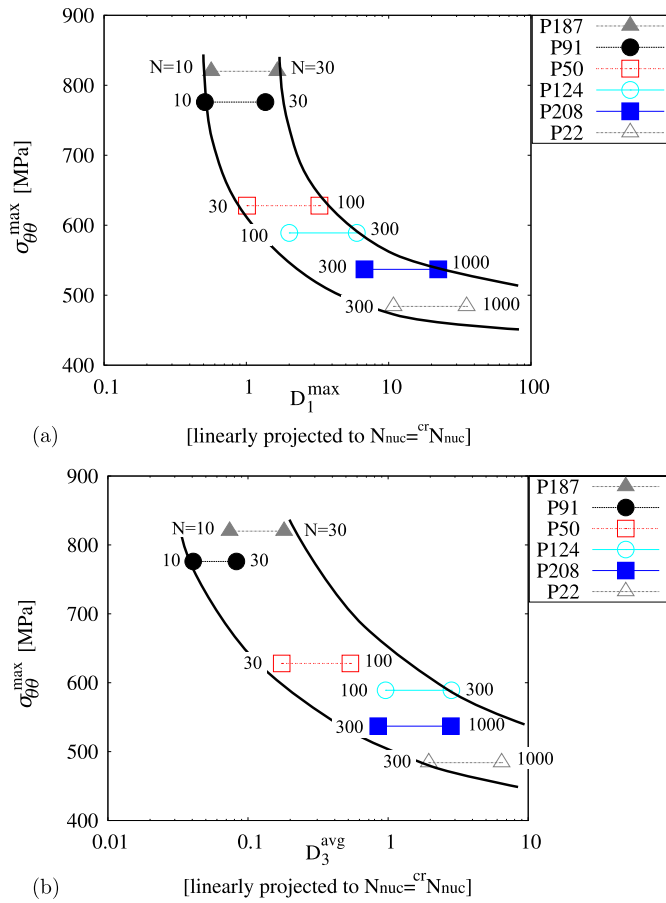
Figure 9. Projected slip-based metrics corresponding to the replication models of particles that were observed to nucleate from the incubated crack (*a*) max($\sigma_{\theta\theta}^{\text{arc}}$) versus D_1 and (*b*) $\sigma_{\theta\theta}^{\text{max}}$ versus D_3^{avg}. Both plots illustrate that the critical stress is dependent on slip accumulation.

in AA7075-T651. In that work, SEM-based stereology in conjunction with EBSD was used to study crack face normal vectors within $50\,\mu$m of the crack-incubating particles (as near the cracked particle as experimentally possible). Two central contributions of that work are shown here in figure 10, where crack facet normal vectors are plotted with respect to crystallographic axes, figure 10(*a*), and specimen coordinates, figure 10(*b*). Figure 10(*a*) shows that the measured crack facet normal vectors do not closely relate to any low-index crystallographic poles and that there is a complete absence of crystallographic {1 1 1} slip-plane cracking. Figure 10(*b*) illustrates that the crack facet normal vectors were closely aligned with the loading direction.

The observations of Gupta (2009) are correctly reproduced in the simulation results shown in figure 8 because crack nucleation from the Al_7Cu_2Fe particles is directed normal to the direction of local $\sigma_{\theta\theta}^{\text{max}}$, figure 8, and is not co-aligned with the slip localization, figures 6 and 7. Figure 8 illustrates that the directions of $\sigma_{\theta\theta}^{\text{max}}$, $\theta \approx 90°$, are nearly perpendicular to the direction of applied load. Furthermore, since AA 7075-T651 is a peak-age hardened alloy, stage-I cracking is not expected due to the nonshearable hardening particles (sub-micrometer precipitates) that result from the peak-age processing of the alloy.
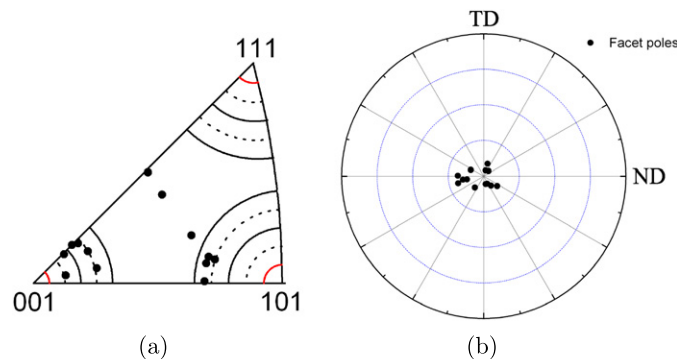
Figure 10. Fatigue crack surface (tested in ambient air environment) crystallography results plotted on (*a*) an irreducible stereographic triangle with contour lines drawn at 3° intervals and (*b*) a stereographic projection with respect to specimen coordinates (Gupta 2009).

The strong dependence of the nucleation stage on the stress field near a cracked particle motivates the mixed-life (stress and strain) fatigue models. The critical-plane model presented in Fatemi and Socie (1988) is one such model and is frequently used as a fatigue indicator parameter for MSFCs. The nonlocal average values of the Fatemi–Socie metric, modified for cyclic loading and crystal plasticity and denoted D_5 in Hochhalter *et al* (2010), are analyzed to relate with previous research, cf McDowell and Dunne (2010). To remain consistent with most previous research, the nonlocal average of the metric and the increment between minimum load and peak load of the metric are analyzed, $\Delta D_5^{\mathrm{avg}}$. The $\Delta D_5^{\mathrm{avg}}$ data in table 4 suggest similar conclusions provided by tables 2 and 3: the $\Delta D_5^{\mathrm{avg}}$ metric can provide predictions for which particles will nucleate a crack, but not when nucleation will occur.

The disparity between $\Delta D_5^{\mathrm{avg}}$ and experiment observations is believed to occur because the stress in the D_5 metric corresponds to the normal stress acting on the slip planes, and not in accordance with the maximum tangential stress, which is found here to have a governing affect on the cycles to nucleation, see figure 9. In other words, since nucleation is a stage-II event in AA 7075-T651, the slip localization and cyclic accumulation locations do not necessarily co-align with the direction of nucleation and, consequently, the maximum tangential stress near the cracked particle should be used to model nucleation.

In addition, predicting the number of cycles to nucleation in the analysis presented here relies on the extrapolation of the slip-based metrics. Extrapolating the cyclic slip accumulation to subsequent load cycles has physical meaning since it is a cumulative process during fatigue loading. However, extrapolating the stress in the same manner is not physical. Therefore, the governing stress component and slip accumulation should be decoupled, with only the slip extrapolated to subsequent load cycles. The main attribute of such a decoupled model is illustrated in figure 9, where the critical stress, as a function of the slip accumulation, can be determined.

The results discussed in this section illustrate that morphology local to a MSFC causes large variation in the stress concentration and slip localization and cyclic accumlation, which govern nucleation and, furthermore, that the size of the incubated crack is not as important at the MSFC nucleation stage. For example, P208 and P91 have equivalent incubated crack sizes; however, P208 nucleated into a stress field where the $\sigma_{\theta\theta}^{\mathrm{max}}$ was about 550 MPa, while P91 nucleated into a stress field where the $\sigma_{\theta\theta}^{\mathrm{max}}$ was about 780 MPa. It is assumed here that the grains are perfectly bonded in each replicated-microstructure model and each polycrystal undergoes the notch-root strain, i.e. the individual grains are locked together and undergo displacement

Table 4. Summary of the replication simulation results for $\Delta D_5^{\mathrm{avg}}$, the nonlocal average of the metric and the increment between minimum load and peak load of the 3rd cycle. The first four particles did not nucleate and, consequently, no cycle range observed for nucleation can be given.

Particle Id	Cycle range	$\Delta D_5^{\mathrm{avg}}$
P11	N/A	1.4E−3
P135	N/A	4.5E−5
P169	N/A	1.4E−3
P88	N/A	1.2E−4
P187	10–30	4.4E−3
P91	10–30	1.5E−2
P50	30–100	2.4E−3
P124	100–300	6.0E−3
P208	300–1000	3.2E−3
P22	300–1000	1.8E−2

controlled deformation. Variation of orientation causes some grains to be relatively stiff with respect to the applied load. Such grains contain a concentrated stress value. This additional concentration of stress led to the relatively early nucleation of the incubated crack in P187, and others that nucleated early, see table 3. Conversely, much more slip accumulation had to occur near the incubated crack in P22, and others that nucleated late, see table 3, expending the neighboring grain's capacity to do plastic work, for the local stress field to be adequate for nucleation.

3.2. Analysis of crack displacement results

Several MSFC propagation stage models are based on the hypothesis that the change in crack-tip displacement over a load cycle, $\Delta\overrightarrow{CTD}$ (a vector representation of the three orthogonal Cartesian components of crack-tip displacement), is the dominant driving force, which is based on experimental observations (Li 1989, 1990, McClintock 1999, McDowell *et al* 2003). It is reasonable then to analyze the relation between $\Delta\overrightarrow{CTD}$ and the nucleation stage. To this end, measured and computed CTD_I values, the opening component, are compared for validation of the microstructure replication simulations, figure 11. Next, computed $||\Delta\overrightarrow{CTD}||$ values for the incubated cracks that nucleated a crack are compared with those that did not nucleate a crack. Lastly, the computed $||\Delta\overrightarrow{CTD}||$ values are compared with the number of cycles required to nucleate an incubated crack.

High-resolution SEM images of five of the monitored particles that incubated a crack were taken at the first load peak—three that nucleated a crack (P124, P187 and P91) and two that did not (P169 and P88). From these images, five CTD_I measurements were taken at the center of the incubated crack, which resulted in a small range of values due to measurement uncertainty, figure 11(*b*). This measured range is given in table 5 along with the corresponding computed CTD_I values. For each, there is close agreement between the measured and computed values.

Along each incubated crack mouth in the replication simulations 100 equally spaced $||\Delta\overrightarrow{CTD}||$ values were queried, starting at point B and ending at point A, figure 12. It is evident from the results, figure 12, that there is a correlation between $||\Delta\overrightarrow{CTD}||$ and actuation of nucleation. Nucleation occurred if the maximum value of $||\Delta\overrightarrow{CTD}||$ along the crack mouth was $>0.060\,\mu$m, and nucleation did not occur if maximum value of $||\Delta\overrightarrow{CTD}||$ along the crack mount was $<0.058\,\mu$m, see figure 12. It was observed during experiment and simulation that CTD_I was nearly constant along most of the crack mouth due to blunting of the incubated crack front, figure 11. Also, the computed values of CTD_I were typically an order of magnitude greater than $CTD_{II,III}$.

20
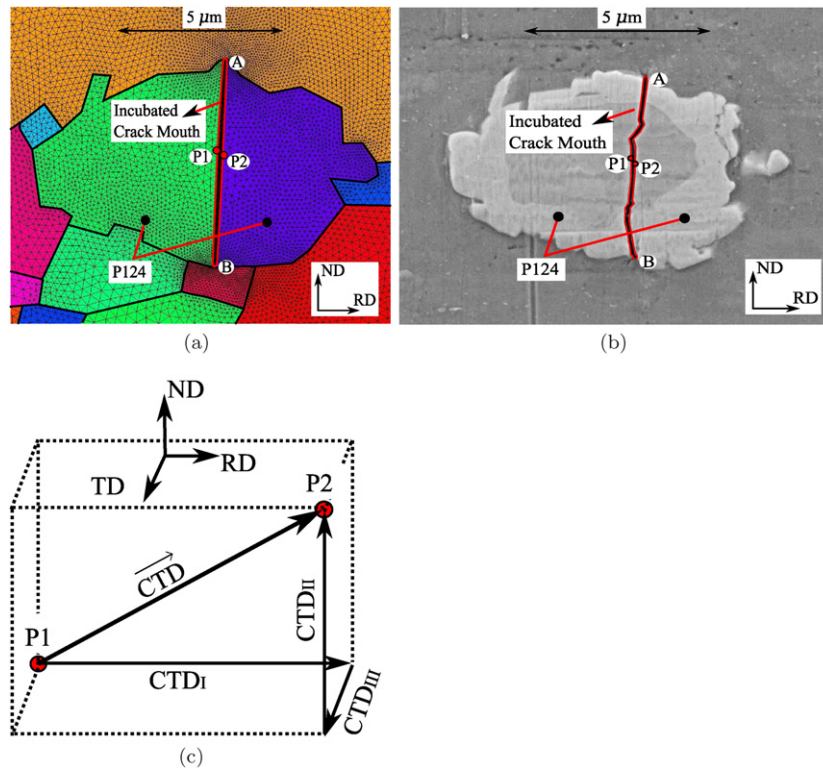
Figure 11. Incubated crack mouth opening in P124 (*a*) simulated and (*b*) observed. (*c*) The vector $\overrightarrow{CTD}$ is the relative displacement of the two sides of the incubated crack with components aligned with the RD, ND and TD.

Table 5. Comparison of the computed and measured CTD values at the first load peak for 5 of the monitored particles that incubated a crack.

Particle Id	P124	P187	P91	P169	P88
Measured CTD_I (μm)	0.12–0.16	0.09–0.11	0.08–0.13	0.05–0.07	0.09–0.11
Computed CTD_I (μm)	0.11	0.10	0.08	0.07	0.07

McClintock (1999) asserted that the ΔCTD_I threshold, ΔCTD_I^{th}, could be approximated by

$$\Delta CTD_I^{th} \approx \frac{2Eb}{\pi \sigma_{ult}}, \tag{5}$$

where E is the elastic modulus, 72 GPa, b is the Burgers vector magnitude, 2.86 Å, and σ_{ult} is the ultimate tensile strength, 570 MPa. Using these values, which are characteristic of AA 7075-T651, equation (5) yields $\Delta CTD_I^{th} = 0.023\,\mu$m, which is about half of the threshold value illustrated in figure 12. Equation (5) is based on a relation between ΔCTD_I and ΔK_I, which was obtained from finite element analysis of microstructurally long cracks. It is expected that ΔCTD_I^{th} obtained from the replication simulations is higher than that predicted by equation (5) because of the presence of nearby microstructural interfaces and more plastic deformation with respect to crack size. Therefore, the measurements and replication simulation results suggest that equation (5) should not be used to predict which incubated cracks are likely to nucleate: more detailed finite element analysis of the microstructure is warranted.

21
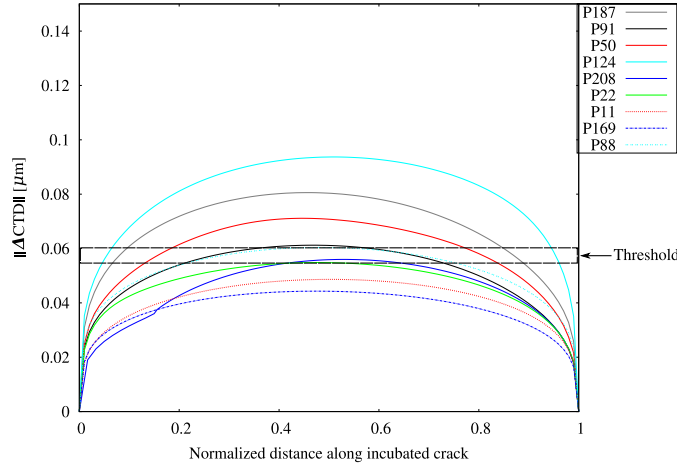
Figure 12. Replication simulation $||\Delta\overrightarrow{CTD}||$ results along the normalized incubated crack mouth opening.

Comparing the number of cycles required to nucleate an incubated crack, table 1, with the computed $||\Delta\overrightarrow{CTD}||$, figure 12, illustrates that high $||\Delta\overrightarrow{CTD}||$ indicates early nucleation with the exception of P124. However, subsequent propagation of the MSFC which nucleated from P124 was observed to have the fastest rate among the monitored particles, which suggests that $||\Delta\overrightarrow{CTD}||$ may be correlated with the rate of MSFC propagation. A subsequent paper in this series will present further analysis pertaining to MSFC propagation, the slip-based metrics, and $||\Delta\overrightarrow{CTD}||$.

4. Nucleation stage model development

The results of the replication simulations illustrate that either $||\Delta\overrightarrow{CTD}||$ or the slip-based metrics, $D_{1,3}$, along with $\sigma_{\theta\theta}^{\max}$ can be used to predict if, when, and in what direction nucleation will occur. The slip-based metrics are chosen for model development because of their intrinsic tie to the mechanics of lower length scales. Conceptually, the results of the replication simulations imply that the expenditure of a microstructure's capacity to do plastic work can be modeled using the slip-based metrics and that $\sigma_{\theta\theta}^{\max}$ will drive the nucleation event, that is, if a critical amount of plastic exhaustion has occurred. This result motivates a model for the nucleation stage. The discussion here will use the computed $D_1^{\max}$ metric as an example, since there is a more well-defined correlation with the number of cycles to nucleation, figure 9(*a*). However, the following development can be used for any of the five slip-based metrics defined in Hochhalter *et al* (2010).

The results of the replication simulations suggest that a power-law relation exists between $^{\mathrm{cr}}\sigma_{\theta\theta}^{\max}$ and the accumulated slip, $D_1^{\max}$, near an incubated crack, figure 13(*a*). For the stress near a cracked particle, $\sigma_{\theta\theta}^{\max}$, to be sufficient for nucleation, a corresponding critical amount of slip must accumulate. This critical relation is given by

$$\sigma_{\theta\theta}^{\max} = {}^{\mathrm{cr}}\sigma_{\theta\theta}^{\max} = \sigma_{\theta\theta}^{\mathrm{ult}}({}^{\mathrm{cr}}D_1^{\max})^{\eta}, \tag{6}$$

where η is a scaling exponent and $\sigma_{\theta\theta}^{\mathrm{ult}}$ is the magnitude of stress capable of driving nucleation with minimal slip accumulation. These two parameters must be calibrated to the data of figure 9(*a*): calibration to the lower-bound data gives $\sigma_{\theta\theta}^{\mathrm{ult}} = 690$ MPa and calibration to the
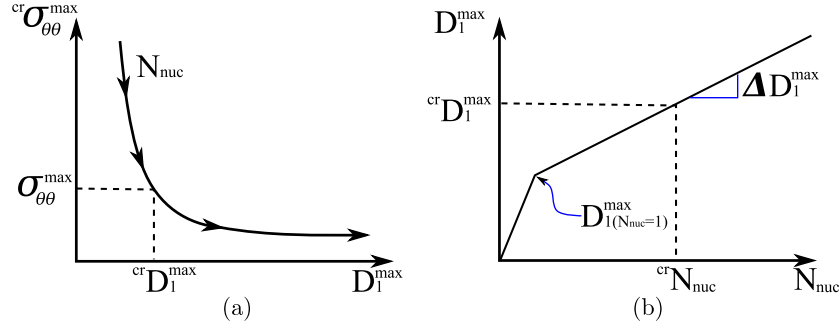
Figure 13. Illustration of the relationships governing the number of cycles to nucleate an incubated crack, $^{cr}N_{nuc}$. (*a*) $^{cr}\sigma_{\theta\theta}^{max}$ decreases as slip is accumulated. The value of $\sigma_{\theta\theta}^{max}$ near an incubated crack is sufficient to drive nucleation only when the critical amount of slip has accumulated, $^{cr}D_1^{max}$. (*b*) $^{cr}D_1^{max}$ for the computed $\sigma_{\theta\theta}^{max}$ near an incubated crack is used to calculate $^{cr}N_{nuc}$.

upper-bound data gives $\sigma_{\theta\theta}^{ult} = 810\,\mathrm{MPa}$, both result in $\eta = -0.15$. As an alternative to fitting $\sigma_{\theta\theta}^{ult}$ to the results given in the previous section, either of the values of $\sigma_{\theta\theta}^{max}$ for the monitored particles that nucleated first, P187 and P91, could be used since little slip had accumulated at the time of nucleation.

From the replication simulation results presented by Hochhalter *et al* (2010), it is assumed to be a first-order approximation that the accumulation of D_1^{max} follows the piecewise-linear form illustrated in figure 13(*b*). This critical relation is given by

$$^{cr}D_1^{max} = D_{1(N_{nuc}=1)}^{max} + \Delta D_1^{max}(^{cr}N_{nuc} - 1), \qquad ^{cr}N_{nuc} \geqslant 1 \tag{7}$$

where N_{nuc} is the number of cycles after incubation and $^{cr}N_{nuc}$ is the number of cycles required to nucleate an incubated crack. Substituting equation (7) into equation (6) gives the semi-empirical model for $^{cr}N_{nuc}$:

$$^{cr}N_{nuc} = \frac{\left(\dfrac{\sigma_{\theta\theta}^{max}}{\sigma_{\theta\theta}^{ult}}\right)^{\frac{1}{\eta}} - D_{1(N_{nuc}=1)}^{max}}{\Delta D_1^{max}} + 1. \tag{8}$$

The model for the number of cycles required to nucleate an incubated crack, given by equation (8), incorporates both the driving force for nucleation, $\sigma_{\theta\theta}^{max}$, as well as the rate at which the surrounding microstructure is expending its capacity to do plastic work, ΔD_1^{max}. As $\sigma_{\theta\theta}^{max}$ increases, $^{cr}N_{nuc}$ decreases. Likewise, as ΔD_1^{max} increases, $^{cr}N_{nuc}$ decreases. The values $\sigma_{\theta\theta}^{max}$, $D_{1(N_{nuc}=1)}^{max}$ and ΔD_1^{max} depend on particle geometry, surrounding grain geometry and orientation, and strain level. According to the model developed here, every incubated crack will eventually nucleate a crack, if $\Delta D_1^{max} \geqslant 0.0$. However, in an actual microstructure, nearby cracks that nucleated relatively early will shield neighboring incubated cracks. Therefore, it is reasonable to set an upper threshold to ^{cr}N, or to explicitly simulate multiple cracked particles within a single model to account for interaction effects.

5. Limitations and alternatives

It is well known that conventional crystal plasticity (CCP) formulations do not accurately capture some aspects of plastic deformation at or below the micrometer-scale. Encompassing discussion of the limitations of crystal plasticity is given by Buchheit *et al* (2005) and Hutchinson (2000). Nevertheless, CCP formulations are commonly employed to study
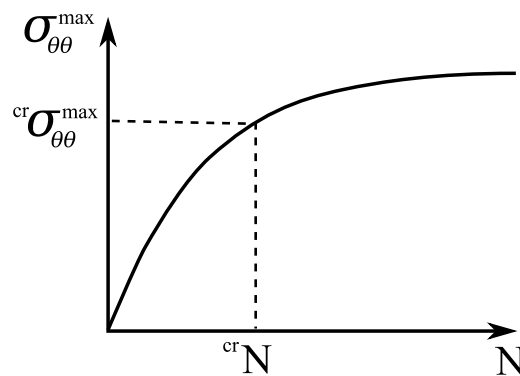
Figure 14. Illustration of attaining a $\sigma_{\theta\theta}^{\max}$ cracking criterion, analogous to that presented herein, for dislocation dynamics models. Stress will increase during the accumulation of dislocation near the crack. Thus, instead of modeling energy dissipation as is done herein via the nucleation metrics, a single constant critical stress is defined and nucleation will occur from a cracked particle once that critical stress is attained.

material state fields near a crack within a microstructure. The physical justification is that valid insight can still be gained as long as the limitations of CCP models are considered, which motivates the use of the nonlocal techniques employed here. One possible approach for determination of a lower bound on the length scale at which CCP formulations begin to break down is presented by Wallin *et al* (2008). In that study, a discrete dislocation region surrounding a crack tip was coupled to a surrounding region represented by CCP. Initially, the discrete dislocation region was made sufficiently large, so that no discrepancy in the resulting stress fields was observed on either side of the coupled boundary. Subsequently, the discrete dislocation region was reduced until a discrepancy was observed, i.e. the length scale at which CCP no longer accurately modeled the stress field, on average. Capability for three-dimensional modeling of discrete dislocations in high-strength alloys is under development (Zbib and Diaz de la Rubia 2002, Arsenlis *et al* 2007, Bulatov 2008). Currently, that approach is limited for the replication models studied herein, but may provide useful qualitative information.

The power-law parameters from section 3 could be explained through more fundamental physics-based consitutive models for dislocation interaction. However, the model developed in this study, which is CCP-based, has a fundamentally different perspective than modeling crack nucleation using dislocation dynamics, cf Groh *et al* (2008). First, nucleation modeling based on CCP models must account for the expenditure of the material's capacity to do plastic work during cyclic loading, i.e. the local material strength is continually reduced by slip accumulation. On the other hand, as illustrated by figure 14, dislocation dynamics and strain-gradient crystal plasticity models incorporate additional work-hardening due to geometrically necessary dislocations (GNDs), thereby cyclically increasing the driving stress until the critical stress is met. The first method accounts for cyclic slip accumulation as an effect on the material's inherent crack growth resistance force, while the second method accounts for GND accumulation as an effect on the crack growth driving force.

6. Summary and conclusions

The development of a mechanistic and probabilistic MSFC simulation methodology is presented throughout this series of papers. In the first paper of the series, Bozek *et al* (2008)

developed a methodology to provide a statistical distribution of Al_7Cu_2Fe particles that are likely to incubate a crack, given distributions of particle shape and surrounding grain orientation. In the second paper of this series, nonlocal slip-based metrics were defined, and numerical issues and physical validity were investigated. These metrics along with the finite element simulations of replicated AA 7075-T651 microstructures analyzed in this third paper provide physical inference of the observed nucleation stage.

The replicated-microstructure simulation results provide insight into the microstructural mechanics governing nucleation upon which a semi-empirical model is developed for predicting the subset of cracked particles that are likely sites for nucleation, the number of cycles required for nucleation, and the nucleation direction. Therefore, the particles in a digital microstructure realization that are likely to incubate and nucleate MSFCs can be predicted, given statistics of inherent microstructure features and local strain level. These particles, which serve as MSFC 'hot spots' in AA 7075-T651, can subsequently be considered in simulations of MSFC propagation, and the statistically insignificant particles can be disregarded.

The semi-empirical model is based on several conclusions, supported by the results of the replicated-microstructure simulations:

(i) Cyclic accumulation rate of slip-based metrics can be used to model which incubated cracks are likely to nucleate, but does not accurately model the number of cycles to nucleate a crack.
(ii) The local maximum tangential stress, $\sigma_{\theta\theta}^{\max}$, acts as the driving force and should be incorporated to model accurately the number of cycles to nucleate an incubated crack.
(iii) The slip-based metrics provide a basis to calculate reduction in local critical driving stress required to nucleate an incubated crack due to cyclic slip accumulation.
(iv) The nucleation direction is normal to the computed, local, maximum tangential stress direction and the observed crack path tortuosity is apparently due to the altering of the direction of maximum tangential stress due to local heterogeneous features. This is consistent with observations of stage-II cracking in peak- and over-aged alloys, where multiple-slip rather than single-slip is dominant.

Several previous observations have shown that small crack growth was characterized by abrupt changes in growth rate (Lankford 1982, Chan and Lankford 1983, Lankford *et al* 1984). It is evident that abrupt changes in growth rate can occur because of mechanisms similar to those governing nucleation: MSFCs must cross microstructural barriers by accumulating slip and having a sufficient local stress. As a MSFC propagates through the AA 7075-T651 microstructure, it navigates regions with widely varying stress fields and levels of accumulated slip. The availability of any paths that are already highly disordered, such as subgrain boundaries, provides an equivalent to a region with highly accumulated slip, i.e. the inherent ability to do plastic work is low. Future work should include an identification of the grain orientations with respect to loading direction that sustain a sufficiently high slip-accumulation rate to promote nucleation without physically restricting tensile stress concentrations, which would lead to early nucleation.

References

Arakere N K, Siddiqui S and Ebrahimi F 2009 *Int. J. Solids Struct.* **46** 3027–44

Arsenlis A, Cai W, Tang M, Rhee M, Oppelstrup T, Hommes G, Pierce T and Bulatov V 2007 *Modelling Simul. Mater. Sci. Eng.* **15** 553–95

Bennett V P and McDowell D L 2003 *Int. J. Fatigue* **25** 27–39

Bowles C Q and Schijve J 1973 *Int. J. Fract.* **9** 171–7

Bozek J E *et al* 2008 *Modelling Simul. Mater. Sci. Eng.* **16** 065007

Brahme A, Alvi M, Saylor D, Fridy J and Rollett A 2006 *Scr. Mater.* **55** 75–80

Brockenbrough J R, Hinkle A J, Magnusen P E and Bucci R J 1994 C Harris (ed) *Proc. FAA/NASA Int. Symp. on Advanced Structural Integrity Methods for Airframe Durability and Damage Tolerance (Hampton, VA)* vol NASA Conference Publication 3274, Part I pp 71–84

Buchheit T E, Wellman G W and Battaile C C 2005 *Int. J. Plast.* **21** 221–49

Bulatov V 2008 Crystal plasticity from dislocation dynamics *Materials Issues for Generation IV Systems (NATO Science for Peace and Security Series B: Physics and Biophysics)* ed V Ghetta, D Gorse, D Mazière and V Pontikis (Dordrecht: Springer) pp 275–84

Chan K S 2003 *Metall. Mater. Trans.* A **34** 43–58

Chan K S 2010 *Int. J. Fatigue* **32** 1428–47

Chan K S and Lankford J 1983 *Scr. Metall.* **17** 529–32

Chang R, Morris W L and Buck O 1979 *Scr. Metall.* **13** 191–4

Dunne F P E, Wilkinson A J and Allen R 2007 *Int. J. Plast.* **23** 273–95

Fan J, McDowell D L, Horstemeyer M F and Gall K 2001 *Eng. Fract. Mech.* **68** 1687–706

Fatemi A and Socie D F 1988 *Fatigue Fract. Eng. Mater. Struct.* **11** 149–65

Fatemi A and Yang L 1998 *Int. J. Fatigue* **20** 9–34

Flouriot S, Forest S, Cailletaud G, Köster A, Rémy L, Burgardt B, Gros V, Mosset S and Delautre J 2003 *Int. J. Fract.* **124** 43–77

Fridline D 2007 'Bethpage, NY: Northrop Grumman Corp.' personal communication

Gall K, Horstemeyer M F, Degner B W, Mcdowell D L and Fan J 2001 *Int. J. Fract.* **108** 207–33

Garrett G G and Knott J F 1975 *Acta Metall.* **23** 841–8

Groh S, Olarnrithinum S, Curtin W, Needleman A, Deshpande V and Van der Giessen E 2008 *Phil. Mag.* **88** 3565–83

Grosskreutz J C and Shaw G G 1969 *Proc. 2nd Int. Conf. on Fracture* (London: Chapman and Hall) pp 620–9

Gupta V K 2009 Diffraction-based study of fatigue crack initiation and propagation in aerospace aluminum alloys *PhD Thesis* University of Virginia Charlottesville

Harlow D, Nardiello J and Payne J 2010 *Int. J. Fatigue* **32** 505–11

Hefferan C, Li S, Lind J, Lienert U, Rollett A, Wynblatt P and Suter R 2009 *Comput. Mater. Continua* **14** 209–19

Hochhalter J D, Littlewood D J, Christ Jr R J, Veilleux M G, Bozek J E, Ingraffea A R and Maniatty A M 2010 *Modelling Simul. Mater. Sci. Eng.* **18** 045004

Horton J A and Ohr S M 1982 *J. Mater. Sci.* **17** 3140–8

Hutchinson J W 2000 *Int. J. Solids Struct.* **37** 225–38

Johnston S R, Poterniche G P, Daniewicz S R and Horstemeyer M F 2006 *Fatigue Fract. Eng. Mater. Struct.* **29** 597–609

Kung C Y and Fine M E 1979 *Metall. Trans.* A **10** 603–10

Lankford J 1982 *Fatigue Fract. Eng. Mater. Struct.* **5** 233–48

Lankford J, Davidson D L and Chan K S 1984 *Metall. Trans.* A **15** 1579–88

Laz P J and Hillberry B M 1998 *Int. J. Fatigue* **20** 263–70

LeDonne J E, Neyer S, III C H, Ozdoganlar O and Rollett A 2011 (in preparation)

Li C 1989 *Fatigue Fract. Eng. Mater. Struct.* **12** 59–65

Li C 1990 *Acta Metall. Mater.* **38** 2129–34

Maire E, Buffiere J, Salvo L, Blandin J, Ludwig W and Letang J 2001 *Adv. Eng. Mater.* **3** 539–46

Manonukul A and Dunne F P E 2004 *Proc. R. Soc. Lond.* A **460** 1881–903

Matouš K and Maniatty A M 2004 *Int. J. Numer. Methods Eng.* **60** 2313–33

McClintock F A 1968 On the mechanics of fracture from inclusions *Ductility* (Metals Park, OH: American Society for Metals)

McClintock F A 1999 Considerations for fatigue crack growth relative to crack tip displacement *Engineering Against Fatigue* (Rotterdam: Balkema)

McDowell D and Dunne F 2010 *Int. J. Fatigue* **32** 1521–42

McDowell D L 2007 *Mater. Sci. Eng.* A **468–470** 4–14

McDowell D L, Gall K, Horstemeyer M F and Fan J 2003 *Eng. Fract. Mech.* **70** 49–80

McEvily A J Jr and Johnston T L 1967 *Int. J. Fatigue* **3** 45–74

Morris W L and James M R 1980 *Metall. Trans.* A **11** 850–1

Murakami Y and Endo M 1994 *Int. J. Fatigue* **16** 163–82

Patton G, Rinaldi C, Brechet Y, Lormand G and Fougeres R 1998 *Mater. Sci. Eng.* A **254** 207–18

Payne J, Welsh G, Christ R J Jr, Nardiello J and Papazian J M 2010 *Int. J. Fatigue* **32** 247–55

Pelloux R M N 1969 *ASM Trans. Q.* **62** 281–5

Potirniche G P and Daniewicz S R 2003 *Int. J. Fatigue* **25** 877–84

Przybyla C, Prasannavenkatesan R, Salajegheh N and McDowell D L 2010 *Int. J. Fatigue* **32** 512–25

Santner J S and Eylon D 1979 *Metall. Trans.* A **10** 841–8

Shenoy M M, Kumar R S and McDowell D L 2005 *Int. J. Fatigue* **27** 113–27

Suresh S 1998 *Fatigue of Materials* (Cambridge: Cambridge University Press)

Tanaka K and Mura T 1981 *J. Appl. Mech.* **48** 97–103

Tanaka K and Mura T 1982a *Mech. Mater.* **1** 63–73

Tanaka K and Mura T 1982b *Metall. Trans.* A **13** 117–23

Tanaka K and Mura T 1984 *Acta Metall.* **32** 1731–40

Templin R L 1954 Third Gillett Lecture *Proc. 57th American Society for Testing of Materials* (Philadelphia, PA: ASTM) pp 2–4

Tóth L S, Molinari A and Zouhal N 2000 *Mech. Mater.* **32** 99–113

Wallin M, Curtin W, Ristinmaa M and Needleman A 2008 *J. Mech. Phys. Solids* **56** 3167–80

Wang L, Daniewicz S, Horstemeyer M, Sintay S and Rollett A 2009 *Int. J. Fatigue* **31** 651–8

Weiland H, Nardiello J, Zaefferer S, Cheong S, Papazian J and Raabe D 2009 *Eng. Fract. Mech.* **76** 709–14

Xue Y, McDowell D L, Horstemeyer M F, Dale M H and Jordon J B 2007a *Eng. Fract. Mech.* **74** 2810–23

Xue Y, Kadiri H E, Horstemeyer M F, Jordon J B and Weiland H 2007b *Acta Mater.* **55** 1975–84

Zbib H and Diaz de la Rubia T 2002 *Int. J. Plast.* **18** 1133–63

Zhang J, Prasannavenkatesan R, Shenoy M M and McDowell D L 2009 *Eng. Fract. Mech.* **76** 315–34